HO_2 reaction kinetics in an atmospheric pressure plasma jet determined by cavity ring-down spectroscopy

HO_2 reaction kinetics in an atmospheric pressure plasma jet determined by cavity ring-down spectroscopy

M. Gianella[1], S. Reuter[2,3], S A Press[1], A Schmidt-Bleker[3], J H van Helden[3] and G A D Ritchie[1]

[1] Department of Chemistry, Physical and Theoretical Chemistry Laboratory, University of Oxford, South Parks Rd, Oxford OX1 3QZ, United Kingdom
[2] Princeton University, Department of Mechanical and Aerospace Engineering, E-Quad, Olden Street, 08542, Princeton, NJ, USA
[3] Leibniz Institute for Plasma Science and Technology (INP), Felix-Hausdorff-Str. 2, 17489 Greifswald, Germany

E-mail: jean-pierre.vanhelden@inp-greifswald.de, stephan.reuter@inp-greifswald.de

Abstract. Hydroperoxyl (HO_2) is detected in the effluent of an atmospheric pressure plasma jet by cavity ring-down absorption spectroscopy. Laser radiation at 1506.4 nm is used to determine HO_2 concentrations directly in the plasma effluent at atmospheric pressure as well as indirectly after sampling through a pinhole and expanding to 5.33 kPa. To unravel the HO_2 reaction kinetics, the argon feed gas is humidified and the plasma jet is equipped with a gas curtain device that controls the surrounding atmosphere. Varying the curtain gas composition from pure nitrogen to pure oxygen leads to a five to six-fold increase in HO_2 concentrations towards higher oxygen concentrations. A reaction kinetics model considering near-field and far-field reactions describes the reaction pathways that determine the hydroperoxyl concentration and is in good agreement with the measurements at both low and atmospheric pressure.

Submitted to: *Plasma Sources Sci. Technol.*

1. Introduction

Cold non-equilibrium atmospheric pressure plasma jets are an emerging technology with wide applicability in fields such as localized materials processing, plasma agriculture, and plasma medicine [1, 2, 3, 4]. Here, the high reactivity at near ambient temperature is exploited in non-destructive interactions with heat sensitive materials or biological systems. Transient radical species strongly influence the chemical reactivity of these plasmas, while their high reactivity can also lead to large concentration gradients. Despite the ever-growing applications of cold (yet reactive) molecular plasmas, many fundamental questions regarding the plasma chemical kinetics remain to be explored; in particular, the physical and chemical interactions of plasmas with solids and liquids. The successful use of plasma jets in the field of plasma medicine [5] – for example in plasma-assisted wound healing – provides a strong motivation to find ways to control the reactive species composition generated by these types of plasma. It is therefore essential to diagnose the fluxes of the generated species, to identify the relevant reaction pathways, to be able to tailor the products for specific biomedical applications, and to gain further insight into plasma-induced reactivity in condensed matter systems. Recent studies have shown that a tailoring of the reactive species composition from nitrogen to oxygen-dominated species is possible [6]. This has important consequences as it is generally believed that the reactive oxygen and nitrogen species (RONS) play a key role in the plasma-driven effects in biological tissue. One of the most important reactive species involved is the hydroxyl radical, OH, a primary product of electron impact dissociation of H_2O. OH drives much of the low temperature oxidation chemistry and in the case of low temperature atmospheric pressure plasmas is an important precursor in the formation of H_2O_2, another interesting RONS with high reactivity and oxidizing capacity within biological samples, and which has been identified at high concentration in the liquid phase [4]. Both OH and H_2O_2 have received much attention in the atmospheric pressure plasma literature. Intimately linked to the reaction chemistry is the hydroperoxyl radical, HO_2, which may also play an important role in plasma medical applications. The hydroperoxyl radical is the protonated form of superoxide anion, O_2^-, that has been identified to play a role in acidification of plasma treated liquids. The reaction $HO_2 \leftrightarrow H^+ + O_2^-$ has a pK_a value of 4.8, which means that in most plasma treated liquid media, HO_2 will transform to superoxide anion. HO_2 is a precursor for many biologic oxidation reactions from lipid peroxidation to inactivation of membrane bound catalase through formation of singlet molecular oxygen. HO_2 is readily formed in the plasma effluent by the rapid reaction of H atoms formed from the dissociation of H_2O with O_2 present in the atmosphere or in the supplied gas curtain. This paper highlights the importance of HO_2 in these cycles by making the first quantitative observations of the concentration of HO_2, $[HO_2]$, as a function of the concentration of O_2, $[O_2]$.

Due to their small spatial dimensions, these jets, however, are difficult to diagnose quantitatively. To characterize the fluxes of the most abundant molecular species and selected atomic species (e.g., Ar and He metastables) generated by these plasma sources,

absorption spectroscopy has become a popular method as it has several advantages over other optical diagnostic techniques, the main one being that it returns absolute number densities providing that the absorption cross-section is known [7]. However, the generally small geometry of the effluent of a plasma jet (in the μm to cm range) severely limits the sensitivity of absorption spectroscopy, especially for highly reactive transient species. To overcome the difficulty of small absorption lengths, cavity-enhanced spectroscopies are a promising class of techniques for localized measurements of compounds with low abundances or weak absorption cross-sections in atmospheric pressure plasma jets. Since the introduction of cavity ring-down spectroscopy (CRDS) for absorption measurements of gaseous samples in 1988 [8], a wide class of cavity-enhanced techniques have been developed for probing solids, liquids, gases, and plasmas, such as CRDS, off-axis cavity-enhanced absorption spectroscopy (OA-CEAS or integrated cavity output spectroscopy (ICOS)), optical feedback cavity-enhanced absorption spectroscopy (OF-CEAS) and noise-immune cavity-enhanced optical heterodyne molecular spectroscopy (NICE-OHMS) [9, 10]. All these techniques are based on the principle of coupling light into a high-finesse optical cavity, which in its simplest form consists of two highly reflective mirrors enclosing the sample under investigation. By measuring the light intensity leaking out of the optical cavity with and without absorbing medium, the concentration of absorbing species can be obtained with detectable concentrations at the parts-per million (ppm) to the parts-per-trillion (ppt) levels [11]. By employing high finesse optical cavities, effective absorption path lengths of several tens of km can be achieved with small base lengths in a small volume. Of all the cavity-enhanced techniques, CRDS has been the most widely used for the detection of species in plasmas; an overview of the applications of pulsed CRDS to characterize various types of atmospheric pressure plasma jets can be found in Zaplotnik *et al.*, with studies concentrating primarily on the detection of N_2^+, N_2(A), OH, and He^* species [12].

Recently we have reported on the detection of HO_2 in the effluent of a mm sized atmospheric pressure plasma jet, the so-called *kINPen-Sci*, using the continuous wave (cw) based method of optical feedback cavity-enhanced absorption spectroscopy [13]. In that article, we showed the dependence of the HO_2 concentration on the feed gas humidity. Here, we build upon these initial results and report on the chemical network responsible for the plasma-generated HO_2. In particular, we determine the effect of O_2 in the curtain gas on the production (or destruction) of HO_2. To measure HO_2, we employ CRDS using a diode laser at 6638.2 cm^{-1} as the light source to probe transitions in the first vibrational overtone of the O − H stretch, i.e. the $2v_1$ band (centred at 6649 cm^{-1}) [14, 15, 16, 17, 18]. We used CRDS instead of OF-CEAS in the current study for a number of reasons. The implementation of CRDS is less complex, while the method is more robust. As a result, the derivation of absorption spectra is more straightforward and less prone to systematic errors. For example, the issue of a fluctuating baseline that we had in the OF-CEAS measurements does not occur here. Importantly, with CRDS, a broader spectral range could be measured, enabling the H_2O absorption lineshapes to be fully resolved; this could not be achieved with the OF-CEAS setup presented

previously, and limited our ability to fit the data. Overall, the acquisition time for CRDS is much faster and the method even more sensitive than OF-CEAS. Using a Ar/H_2O mixture as the feed gas, the dependence of $[HO_2]$ on the oxygen fraction in the curtain gas surrounding the plasma jet was investigated. The plasma discharge operates at atmospheric pressure, but measurements of $[HO_2]$ were acquired both at atmospheric pressure and at 5.33 kPa. The latter helped to reduce the effect of pressure broadening on the observed spectra and corroborated our conclusions from observations at higher pressure. It also enabled a first indication of the radial profile of the HO_2 densities to be obtained.

The remainder of the paper is structured as follows. In section 2 the plasma jet device is briefly introduced and the CRDS setup is described in detail. In section 3 the procedure employed to derive the experimental $[HO_2]$ from the absorption spectra and the estimation of the HO_2 absorption cross-section are presented. The kinetic model used to predict $[HO_2]$ is illustrated in section 4. The sensitivity of the spectrometer is discussed in section 5.1, followed by the atmospheric pressure measurements (section 5.2) which are evaluated with kinetic modelling. In section 5.4 the low pressure oxygen variation measurements are presented.

2. Experimental Setup

The non-thermal plasma used in this work is an argon atmospheric pressure plasma jet operated at a radio frequency around 1 MHz. The so-called *kINPen-Sci* has a pin-type powered electrode centred in a dielectric tubing with a circular grounded electrode outside the dielectric [19]. The plasma jet is operated at about 1 W dissipated power. It is equipped with a gas curtain device, which allows for control of the atmosphere surrounding its active afterglow and thus the chemical pathways that can occur [20]. Changing the composition of the curtain gas strongly influences the composition of the reactive components generated by the plasma. For instance, humidity variation controls the output of H_2O_2 and OH [21]. The feed gas argon has a flow rate of 3 slm and is humidified by passing a small fraction ($4\,\% - 10\,\%$) through a water bubbler held at room temperature (figure 1c). The feed gas humidity was measured with a chilled mirror dew point hygrometer. The gas curtain is operated with a mixture of O_2 and N_2 at a total flow rate of 5 slm and can be varied from pure O_2 to pure N_2.

A schematic of the CRDS spectrometer is shown in figure 1a. A 1506.4 nm ($6638.2\,cm^{-1}$) distributed feedback laser diode (LD) in a fibre-pigtailed butterfly package (NTT Electronics NLK1S5GAAA) is used as the light source. An inline acousto-optic modulator (Gooch & Housego Fibre-Q) is connected in series between the laser and the adjustable fibre collimation package (Thorlabs CFC-8X-C). The current and temperature of the laser are controlled by a Thorlabs LDC200 current driver and a Thorlabs TED200 temperature controller, respectively. The laser beam is directed into the linear cavity with protected silver mirrors. A $f = 10$ cm focal length lens is employed in combination with the adjustable fibre collimation package to achieve spatial matching

of the beam with the fundamental (Gaussian) transverse mode of the optical cavity. The cavity consists of two highly reflective dielectric mirrors (Layertec, reflectivity ≈ 0.99998, radius of curvature = 1 m). For the atmospheric pressure measurements, the optical cavity is enclosed by an aluminium box with an acrylic glass lid and quartz windows (volume: 36.8 L). The distance between the mirrors is about 80 cm, and the beam in the cavity intercepts the effluent from the plasma jet (PJ) at the cavity's mid-point. The laser beam of 1 mm diameter passed through the plasma effluent at 10 mm distance from the plasma jets nozzle as this is the typical distance between plasma jet and treated surfaces. For the low pressure measurements, the mirrors are housed in home-built stainless steel enclosures connected by a glass tube of length 75 cm (figure 1b). The distance between the mirrors in this case is 86 cm, and the effluent is sampled through a pinhole and expanded to a pressure of 5.33 kPa. The pinhole in a 0.05 mm thick copper sheet ,mounted on a glass nozzle of 25.4 mm length to the main glass tube, has a diameter of approximately 0.1 mm. The vacuum pump is connected to one of the mirror enclosures, and the distance between the pinhole inlet and the outlet towards the pump is 30 cm. In both atmospheric and low pressure setups, the "exit" mirror is mounted on a hollow cylindrical piezoelectric transducer so that the length of the cavity can be modulated by a few laser wavelengths. The light exiting the cavity is focused by a $f = 2.54$ cm lens onto an InGaAs photodiode (Thorlabs DET10C); the photocurrent is then amplified by a transimpedance amplifier (FEMTO DLPCA-200). The amplified photosignal is sent to a home-built trigger circuit which switches the AOM off whenever the signal exceeded a preset threshold, thus initiating a ring-down event. The signal is also fed to a USB data acquisition unit (National Instruments NI-USB 6356) which is triggered by a digital pulse sent by the trigger circuit whenever the AOM is being switched off. The spectrometer is controlled by a custom LabVIEW (National Instruments) program running on a standard PC which is also used for further averaging and processing of the data.

3. Derivation of HO_2 and H_2O number densities from absorption spectra

In CRDS, one measures the total cavity loss rate, which is inversely proportional to the ring-down time (RDT). The loss rate consists of all the possible loss mechanisms: transmission of light through the cavity mirrors, absorption within the dielectric coating of the mirrors, diffraction losses (aperture effect of the finite diameter of the mirrors), scattering by the sample (e.g. due to particulate matter, but also because of refractive index gradients or gas turbulence), and optical absorption. Apart from optical absorption, none of the aforementioned effects exhibits a strong frequency dependence; over the typical range of a measured spectrum (in our case $\sim 1\,\mathrm{cm}^{-1}$), they can thus be modelled with a straight line (we allow a non-zero gradient in the baseline to account for slow changes in the ring-down time, due for example to material depositing on the reflective coating of the mirrors). Unfortunately, at atmospheric pressure there is no easy way of establishing this baseline, since the absorption of HO_2 is rather broad

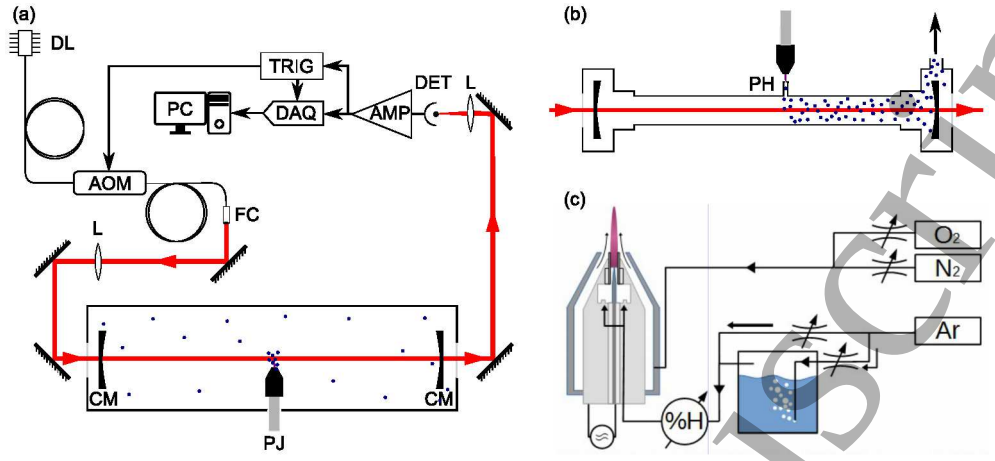

Figure 1: (a) Schematic of the atmospheric pressure CRDS experimental setup with the effluent of the atmospheric pressure plasma intercepting the beam circulating within the linear cavity. DL: diode laser; AOM: acousto-optic modulator; FC: fibre collimation package; L: lens; CM: cavity mirror; PJ: *kINPen-Sci* plasma jet device; DET: photodetector; AMP: amplifier; DAQ: data acquisition module; TRIG: trigger circuit. (b) Linear cavity for low pressure measurements. PH: pinhole. (c) The atmospheric pressure plasma jet *kINPen-Sci* with a gas curtain device operated with a mixture of O_2 and N_2 to control the ambient surrounding the jet afterglow. The feed gas argon is humidified by passing a small fraction through a water bubbler held at room temperature. The feed gas humidity is measured with a chilled mirror dew point hygrometer. %H: hygrometer

and overlapping (see figure 2 later on), and there is a significant contribution from atmospheric water absorption as well. Nevertheless, if the absorption cross-sections of HO_2 and H_2O are known, one can try to fit the measured ring-down spectrum to obtain the number densities:

$$\alpha(\nu) = \frac{1}{c}\left[\frac{1}{\tau(\nu)} - \frac{1}{\tau_0(\nu)}\right] = [\mathrm{H_2O}]\sigma_{\mathrm{W}}(\nu) + \frac{\ell}{L}[\mathrm{HO_2}]\sigma_{\mathrm{H}}(\nu) + \varepsilon(\nu), \qquad (1)$$

where $[H_2O]$, $[HO_2]$ are the molecular number densities of water (W) and HO_2 (H), σ_{W}, σ_{H} are the absorption cross-sections, $\varepsilon(\nu)$ is the residual, $\tau(\nu)$ is the RDT, $\tau_0(\nu)$ encompasses all the loss mechanisms cited above except absorption, and we assume

$$\frac{1}{c\tau_0(\nu)} = b_0 + b_1\nu, \qquad (2)$$

where b_0, b_1 are the baseline coefficients. The fraction ℓ/L takes into account that absorption due to HO_2 is localized over a length ℓ, and L is the cavity length. Water is assumed to be homogeneously distributed over the cavity length.

3.1. Absorption cross-sections of HO_2 *and* H_2O

The absorption cross-section of water can be computed from the line strengths tabulated in the HITRAN database where the pressure-broadening parameter is given in air [22]. In the measurements below, the mixing ratio, Ar:O_2:N_2, of the atmosphere within the cavity volume ranges from 3:0:5 to 3:5:0. By measuring the $(v_1, v_2, v_3; J, K_a, K_c) = (0, 2, 1; 10, 3, 7) \leftarrow (0, 0, 0; 11, 3, 8)$ water transition at $6638.914\,\mathrm{cm}^{-1}$ for various mixing ratios between the aforementioned extremes, an empirical relationship between the pressure-broadening parameter and the mixing ratio was found. The water absorption cross-section was then computed separately for each mixing ratio by using the HITRAN parameters, except for the pressure-broadening parameter for which the empirical value was substituted.

Thiebaud *et al.* have measured the absorption spectrum of HO_2 in $6,67\,\mathrm{kPa}$ of helium [15]. By inspecting their raw spectra and tabulated data, we have visually determined all the significant transitions in the range between $6637.3\,\mathrm{cm}^{-1}$ and $6639\,\mathrm{cm}^{-1}$. We have then determined the position, $\nu_{\mathrm{H}}^{(t)}$, and line strength, $\mathscr{S}_{\mathrm{H}}^{(t)}$, of each transition, t, by applying Gaussian fits to the data. We couldn't extract the pressure-broadening parameters from the raw data, in part because of the small pressure-broadening caused by helium at $6,67\,\mathrm{kPa}$ (the lines are essentially Doppler-broadened), and in part because even at this reduced pressure there is still congestion of absorption lines. We therefore assumed the same pressure-broadening coefficient, γ_{H}, for all transitions. Ibrahim *et al.* have reported air pressure-broadening parameters for 34 HO_2 transitions between $6631\,\mathrm{cm}^{-1}$ and $6671\,\mathrm{cm}^{-1}$ with values ranging from $0.078\,\mathrm{cm}^{-1}\mathrm{atm}^{-1}$ to $0.1548\,\mathrm{cm}^{-1}\mathrm{atm}^{-1}$ (HWHM). With our $Ar/O_2/N_2$ atmosphere, significantly different values should be expected [23]. Next, we calculated the absorption cross-section at the frequency ν due to the transition t as an area-normalized Voigt profile, $\mathscr{V}(\nu - \nu_{\mathrm{H}}^{(t)}; \gamma_{\mathrm{H}})$, multiplied by the transition's line strength:

$$\sigma_{\mathrm{H}}^{(t)}(\nu; \gamma_{\mathrm{H}}) \doteq \mathscr{S}_{\mathrm{H}}^{(t)} \mathscr{V}(\nu - \nu_{\mathrm{H}}^{(t)}; \gamma_{\mathrm{H}}). \tag{3}$$

The absorption cross-section due to all HO_2 transitions at ν then becomes:

$$\sigma_{\mathrm{H}}(\nu; \gamma_{\mathrm{H}}) = \sum_t \sigma_{\mathrm{H}}^{(t)}(\nu; \gamma_{\mathrm{H}}) = \sum_t \mathscr{S}_{\mathrm{H}}^{(t)} \mathscr{V}(\nu - \nu_{\mathrm{H}}^{(t)}; \gamma_{\mathrm{H}}). \tag{4}$$

As an example, figure 2 shows the absorption cross-section of HO_2 computed with equation (4) at $1.01325\,\mathrm{hPa}$ and with the choice $\gamma_{\mathrm{H}} = 0.06\,\mathrm{cm}^{-1}\mathrm{atm}^{-1}$ (half width at half maximum (HWHM)). The peak absorption cross-section of the water transitions in this spectral interval is several orders of magnitude lower ($\sigma_{\mathrm{W}} \sim 10^{-24}\,\mathrm{cm}^2$), but since the water number density is much higher than HO_2, the contribution to the absorption spectrum is significant.

The uncertainty in the HO_2 absorption cross-section arises from the line positions, $\nu_{\mathrm{H}}^{(t)}$, and strengths, $\mathscr{S}_{\mathrm{H}}^{(t)}$, of the HO_2 transitions, extracted from the data [15]. This procedure requires a certain amount of personal judgement, as it is not always clear how many transitions are present within a given congested absorption feature. Furthermore, when the overlap is particularly significant, the uncertainty in both position and strength

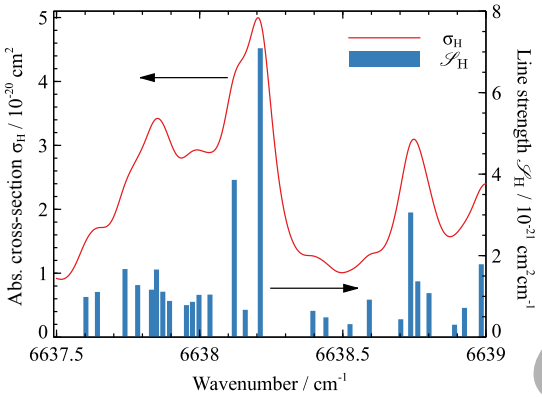

Figure 2: Absorption cross-section of HO_2 computed with equation (4) with the data of Thiebaud *et al.* at 1.01325 hPa and with $\gamma_H = 0.06\,\mathrm{cm^{-1}atm^{-1}}$.

becomes large. A further source of error is due to the assumption that all transitions exhibit the same pressure-broadening parameter, γ_H.

3.2. Fitting

The fit of the spectral data, equation (1), is linear in the four fit parameters, $\boldsymbol{\beta} = [b_0\ b_1\ \mathscr{N}_W\ \mathscr{N}_H]^\top$, with the definitions $\mathscr{N}_W = [H_2O]$ and

$$\mathscr{N}_H = (\ell/L)[HO_2]. \tag{5}$$

The residuals are given by $\varepsilon(\nu) = \mathscr{N}_W\sigma_W(\nu) + \mathscr{N}_H\sigma_H(\nu;\gamma_H) + b_0 + b_1\nu - \frac{1}{c\tau(\nu)}$. The minimum of the residual sum of squares, $\chi^2 \doteq \sum\varepsilon^2$, follows from the condition $\partial\chi^2/\partial\boldsymbol{\beta} = \mathbf{0}$. The latter is a 4×4 system of linear equations of the form,

$$\mathbf{M}\boldsymbol{\beta} = \boldsymbol{\omega}, \tag{6}$$

where $\mathbf{M}$ is a 4×4 real symmetric matrix and $\boldsymbol{\omega}$ is a 4×1 real vector,

$$\mathbf{M} = \begin{bmatrix} N_\nu & \sum\nu & \sum\sigma_W & \sum\sigma_H \\ \cdot & \sum\nu^2 & \sum\sigma_W\nu & \sum\sigma_H\nu \\ \cdot & \cdot & \sum\sigma_W^2 & \sum\sigma_W\sigma_H \\ \cdot & \cdot & \cdot & \sum\sigma_H^2 \end{bmatrix}, \quad \boldsymbol{\omega} = \frac{1}{c}\begin{bmatrix} \sum\tau^{-1} \\ \sum\tau^{-1}\nu \\ \sum\tau^{-1}\sigma_W \\ \sum\tau^{-1}\sigma_H \end{bmatrix}, \tag{7}$$

and the sums go over all frequencies of the spectrum, $\sum x \doteq \sum_{k=1}^{N_\nu} x(\nu_k)$, with N_ν the number of spectral points. For each measurement, the fit vector, $\boldsymbol{\beta}$, was computed with Matlab's `mldivide` command, which performs a robust matrix "inversion" of $\mathbf{M}$. The procedure was repeated for an array of values of the pressure-broadening parameter, and the values of $\boldsymbol{\beta}$ and γ_H yielding the lowest χ^2, $\chi_0^2 \doteq \min_{\gamma_H}\chi^2$, were retained as the best fit values.

The 95 % confidence interval for $\mathscr{N}_H$ was computed with the F-ratio method. Let $\chi_c^2(\mathscr{N}_H)$ denote the residual sum of squares for the (constrained) fit with $\mathscr{N}_H$ held fixed

at some arbitrary value.‡ If the constrained fit is as good as the unconstrained one and the residuals all exhibit a normal distribution with zero mean and constant standard deviation (null hypothesis), then the statistic,

$$F = (N_\nu - 4)\frac{\chi_c^2(\mathscr{N}_\mathrm{H}) - \chi_0^2}{\chi_0^2} \sim F_{1,N_\nu-4}, \tag{8}$$

follows an F distribution with 1 and $N_\nu - 4$ degrees of freedom [24]. The null hypothesis is rejected if $F > F_{1,N_\nu-4}(0.95)$, where $F_{1,N_\nu-4}(0.95)$ denotes the 95-percentile of the $F_{1,N_\nu-4}$ distribution (i.e. the inverse of the cumulative distribution function (of the F distribution) evaluated at 0.95). The 95 % confidence interval for $\mathscr{N}_\mathrm{H}$ is thus defined as the interval,

$$\left\{ \mathscr{N}_\mathrm{H} \left| (N_\nu - 4)\frac{\chi_c^2(\mathscr{N}_\mathrm{H}) - \chi_0^2}{\chi_0^2} \leq F_{1,N_\nu-4}(0.95) \right. \right\}. \tag{9}$$

Note that systematic errors arising from inaccuracies in the absorption cross-section of HO_2 are not taken into account; if systematic errors are present, then the residual's zero-mean assumption in the null hypothesis breaks down and the F-ratio (equation (8)) no longer obeys an F distribution.

In the atmospheric pressure measurements, the high reactivity of HO_2 results in a strong localization of the radical within the active effluent. From quantitative schlieren diagnostics on the plasma jet an absorption length of 4 mm for the plasma effluent at 10 mm distance from the plasma jets nozzle was obtained [25]. If we assume $[HO_2]$ to be homogeneously distributed over a distance $\ell = 4\,\mathrm{mm}$ and zero otherwise [26], the local $[HO_2]$ with a cavity length of $L = 80\,\mathrm{cm}$ is given by $[HO_2] = 200\mathscr{N}_\mathrm{H}$ (see equation (5)).

In the low pressure measurements, we assume $[HO_2]$ to be constant within the glass tube between the pinhole inlet and the mirror on the side where the vacuum pump is connected (i.e. over a length of 30 cm). In this case, the correction factor is $L/\ell = 86/30 \approx 2.9$ and so $[HO_2] = 2.9\mathscr{N}_\mathrm{H}$. This last value represents $[HO_2]$ at 5.33 kPa. The initial concentration generated outside the glass tube at atmospheric pressure is obviously significantly larger; the initial HO_2 number density is reduced due to the expansion from atmospheric pressure to 5.33 kPa by an estimated factor of $760/40 = 19$, but possibly significantly more due to sampling and wall losses, *vide infra.*

4. Reaction kinetics model

4.1. Parametric model for the plasma effluent

A simplified zero-dimensional plug-flow model has been implemented based on the approach presented in [26]. For this, the reaction kinetics equations are solved in a volume element that is co-moving with the flow at its average velocity of $v_0 = 25\,\mathrm{m\,s^{-1}}$. The distance of the volume element from the extremity of the kINPen is then given by $z = v_0 t$, where t is the time. Previously, the influence of feed-gas humidity on the

‡ This constrained fit can be computed in a similar fashion as above by modifying $\mathbf{M}$ and $\boldsymbol{\omega}$ (equation (7)) appropriately.

generation of H_2O_2 and O_3 by the kINPen operated with a shielding gas device was investigated by Fourier transform infrared (FTIR) spectroscopy [27]. It was found, that if the feed gas humidity is increased from dry conditions to 1890 ppm H_2O, the O_3 density decreases from $1.1 \times 10^{14}\,\mathrm{cm}^{-3}$ to $0.1 \times 10^{14}\,\mathrm{cm}^{-3}$, while the density of H_2O_2 increases linearly from zero to $1.3 \times 10^{14}\,\mathrm{cm}^{-3}$ and no other RONS (such as NO_2) were detectable. Since all experiments in the current work are carried out at an even higher feed gas humidity of the oder of 3000 ppm H_2O, the model is based on the assumption that the plasma mainly serves as a source of H and OH while further RONS are generated in negligible amounts.

The dissociation of H_2O can occur via electron impact dissociation

$$e + \mathrm{H_2O} \rightarrow e + \mathrm{H} + \mathrm{OH}$$

or via reaction with electronically excited species, especially Ar^* (e.g. the $Ar(^3P_2)$-state), Ar_2^*, or excited molecular nitrogen (e.g. $N_2(A)$), [28, 29, 30]

$$\mathrm{Ar^*/Ar_2^*/N_2(A) + H_2O \rightarrow H + OH + products.}$$

H and OH can also be generated via further pathways, e.g., involving reactions of H_2O^+ or H_3O^+ with H_2O [31]. In the model, the generation of H and OH is denoted by the fictitious reaction (R0),

$$\mathrm{H_2O \rightarrow H + OH,} \qquad \text{(R0)}$$

with the unknown rate constant k. Reaction (R0) is only active until $t = t_{\mathrm{tip}} = 0.4\,\mathrm{ms}$, corresponding to the volume element having travelled to the tip of the visible plasma effluent, located at a distance $z_{\mathrm{tip}} = v_0 t_{\mathrm{tip}} = 1\,\mathrm{cm}$ in the plug flow model.

The reaction kinetics is computed by solving the system of ordinary differential equations

$$\frac{\mathrm{d}}{\mathrm{d}t}[X](t) = G_X(t) - L_X(t), \qquad (11)$$

where $[X]$ are the number densities of the reactive species in table 1, $X = \mathrm{HO_2}$, $\mathrm{O_2}$, $\mathrm{H_2O}$, H, OH, ... The gain (G_X) and loss (L_X) terms are compiled according to the reactions listed in table 1.

As previously carried out by Schmidt-Bleker *et al.*, the diffusion of the oxygen curtain gas into the active plasma effluent was estimated with the non-dispersive-path-mapping approximation [32, 26], assuming an increase of the oxygen density, $[\mathrm{O_2}](z)$, along the jet axis $z = v_0 t$ by adding the source term in equation (11),

$$G_{\mathrm{O_2}}^{\mathrm{diff}}(t) = [\mathrm{O_2}]_0 \frac{\mathrm{d}}{\mathrm{d}t} \exp\left(-\frac{r_0^2 v_0}{4Dz(t)}\right), \qquad (12)$$

where $r_0 = 0.8\,\mathrm{mm}$ is the radius of the dielectric tube, D the effective diffusion coefficient, and $[\mathrm{O_2}]_0$ is the density of O_2 in the far-field according to a given curtain gas composition. Both the rate coefficient k in equation (R0) and the diffusion coefficient D in equation (12) are used as free parameters to fit the simulated densities of HO_2 to the values obtained experimentally.

Table 1: Set of reactions used in the plug-flow model.

	Reaction	Rate coeff.[a,b]	Reference
(R0)	$H_2O \rightarrow H + OH$	k	
(R1)	$H + O_2 + M \rightarrow HO_2 + M$	2.02×10^{-32}	[33]
(R2)	$H + H + M \rightarrow H_2 + M$	6.00×10^{-33}	[34]
(R3)	$HO_2 + H \rightarrow OH + OH$	6.47×10^{-11}	[34]
(R4)	$HO_2 + H \rightarrow H_2 + O_2$	6.67×10^{-12}	[34]
(R5)	$HO_2 + H \rightarrow H_2O + M$	2.40×10^{-12}	[34]
(R6)	$OH + H + M \rightarrow H_2O + M$	2.56×10^{-31}	[35]
(R7)	$OH + H_2O_2 \rightarrow HO_2 + H_2O$	1.70×10^{-12}	[35]
(R8)	$H_2O_2 + H \rightarrow OH + H_2O$	4.20×10^{-14}	[34]
(R9)	$HO_2 + HO_2 \rightarrow H_2O_2 + O_2$	1.63×10^{-12}	[35]
(R10)	$HO_2 + HO_2 + M \rightarrow H_2O_2 + O_2 + M$	5.00×10^{-32}	[35]
(R11)	$HO_2 + OH \rightarrow H_2O + O_2$	1.10×10^{-10}	[35]
(R12)	$OH + OH + M \rightarrow H_2O_2 + M$	6.16×10^{-31}	[33]

[a] The units of the rate coefficients are $cm^3\,s^{-1}\,molecule^{-1}$ for two-body reactions, $cm^6\,s^{-1}\,molecule^{-2}$ for three-body reactions, and s^{-1} for (R0). A temperature of 300 K was assumed.

[b] M denotes a third body with a density of $2.44 \times 10^{19}\,molecule\,cm^{-3}$. If the respective reaction coefficient was available, Ar was chosen as third body.

5. Results and Discussion

5.1. Sensitivity of the spectrometer

Figure 3 shows an Allan-Werle plot measured with the evacuated cavity [36]. The ring-down rate was $125\,s^{-1}$, and the data for figure 3 was acquired over about 2 h. The Allan deviation of α for an averaging time of 1 s is $3.8 \times 10^{-11}\,cm^{-1}$ (under ideal conditions). At atmospheric pressure, this corresponds to the absorption (at $6638.20\,cm^{-1}$) caused by a homogeneous distribution of HO_2 of $7.4 \times 10^8\,molecule\,cm^{-3}$ (absorption cross-section $\sigma_H \approx 5 \times 10^{-20}\,cm^2$), or alternatively, $1.5 \times 10^{11}\,molecule\,cm^{-3}$ of HO_2 if the molecules are localized within a volume with a diameter of 4 mm. At 5.33 kPa, the absorption cross-section is $\sigma_H \approx 3.2 \times 10^{-19}\,cm^2$, and the value becomes $1.2 \times 10^8\,molecule\,cm^{-3}$ (for the homogeneous distribution). The actual sensitivity to HO_2 when the plasma jet is active in the atmospheric pressure measurements is worse by about one order of magnitude because the plasma interferes with the operation of the cavity by introducing random fluctuations in the cavity losses (e.g., because of gas turbulence and variations in the refractive index). The sensitivity however significantly improves at low pressure and approaches that of the evacuated cavity as the small flow that is being sampled by the pinhole does not perturb the circulating light wave within the cavity. Furthermore, the absorption cross-section of HO_2 increases from $5 \times 10^{-20}\,cm^2$ at 1.01325 hPa to $3.2 \times 10^{-19}\,cm^2$ at 5.33 kPa. A drawback, however, is that the initial $[HO_2]$ produced at

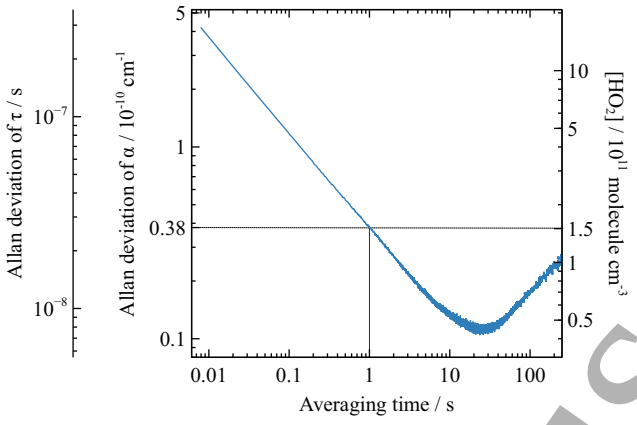

Figure 3: Allan-Werle plot, showing the uncertainty in the ring-down time, in the absorption coefficient, and in the HO_2 number density. The HO_2 number density was computed assuming an absorption cross-section of $5 \times 10^{-20}\,\mathrm{cm}^2$ and a sample with a diameter of 4 mm.

atmospheric pressure is significantly reduced due to expansion and sampling as well as wall losses.

5.2. Atmospheric pressure measurements

For our study of the influence of shielding gas composition on the HO_2 concentration, two runs were performed where the volume fraction of O_2 was varied from: (1) $f = 0\,\%$ (pure N_2) to $f = 100\,\%$ (pure O_2) in steps of 20 %; (2) from $f = 100\,\%$ to $f = 0\,\%$ in steps of $-20\,\%$. The N_2 fraction was always $1 - f$, so that the total curtain gas flow was kept constant. The full set of absorption spectra for the first run is shown in figure 4. The HO_2 and H_2O number densities for both runs were computed in the following fashion. Since the pressure-broadening parameter for HO_2, γ_H, is unknown, the absorption cross-section of HO_2, σ_H (equation (4)), was computed for a range of values of γ_H, namely $0.015\,\mathrm{cm}^{-1}\mathrm{atm}^{-1} \leq \gamma_\mathrm{H} \leq 0.095\,\mathrm{cm}^{-1}\mathrm{atm}^{-1}$. For each value of γ_H, the best fit to the measured spectrum was computed by solving equation (6) with respect to $\boldsymbol{\beta}$. Of all the fits (one for each value of γ_H), the one yielding the smallest χ^2 (i.e. the best fit in the least-squares sense) was retained.

Figure 5 shows the average (of the two runs) $[HO_2]$ in the measurement cell as a function of O_2 fraction in the curtain gas, f. The number densities, assumed to be homogeneous over the 4 mm diameter of the effluent and zero without, were computed with equation (5). For comparison, the results of a similar measurement series taken at an earlier date with an OF-CEAS spectrometer are also shown. The two curves are in very good agreement; with $f = 0\,\%$, the HO_2 number density was about $1.5 \times 10^{13}\,\mathrm{molecule\,cm}^{-3}$, increasing quickly to $5 \times 10^{13}\,\mathrm{molecule\,cm}^{-3}$ at $f = 20\,\%$, and then more slowly to about $8 \times 10^{13}\,\mathrm{molecule\,cm}^{-3}$ at $f = 100\,\%$. The error bars

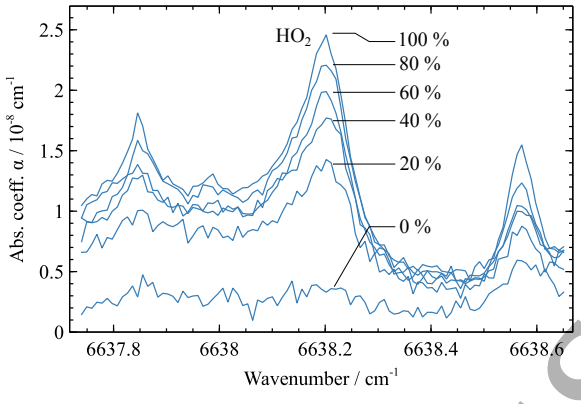

Figure 4: Measured CRDS spectra for shielding gas oxygen fractions of $f = 0, 20, 40, 60, 80$, and $100\,\%$.

are the $95\,\%$ confidence intervals determined with the F-ratio method (see section 3.2). Also shown in figure 5 are the values of γ_H for which the best fit was obtained for each O_2 fraction value. When comparing both spectrometers, significant differences in the values of γ_H are obtained. The spectra taken with the OF-CEAS setup were limited in the spectral range that could be recorded, while also having a fluctuating baseline. As a result, the water absorption lines could not be resolved fully, which hampered the accuracy of the fitting procedure and this mostly affected the value for the pressure-broadening parameter. The CRDS method enabled us to record a much broader spectral range and as a result, the water absorptions could be resolved fully as is show in figure 4. Now, the fitting procedure returned much more consistent values for the pressure-broadening parameters, which turned out to be consistently larger than the values determined with the OF-CEAS method. As the CRDS spectra have a much better signal-to-noise ratio, we believe that the pressure-broadening parameters derived by this method are a better representation of the broadening observed with a gas mixture of $Ar/O_2/N_2$. The decrease of γ_H with increasing oxygen concentration is consistent with the three times smaller electric quadrupole moment of O_2 compared to N_2 (assuming that the attractive inter-molecular forces play a role in the pressure broadening) [37]. Moreover, the present values lie below the range of air-broadened values reported by Ibrahim *et al.* ($0.078\,\mathrm{cm^{-1}atm^{-1}} \leq \gamma_H \leq 0.1548\,\mathrm{cm^{-1}atm^{-1}}$ for 34 transitions in the range $6631\,\mathrm{cm^{-1}} - 6671\,\mathrm{cm^{-1}}$) and above the helium-broadened values determined by Assaf *et al.* ($\gamma_H = 0.031\,\mathrm{cm^{-1}atm^{-1}}$ for the transition at $7000.28\,\mathrm{cm^{-1}}$) [23, 38]; this, again, is consistent with the fact that argon-induced broadening is weaker than N_2-broadening (which is the dominant effect in air) but stronger than He-induced broadening (Ar is more polarisable than He).

The spectra and fits to the CRDS data for $f = 0\,\%$ and $f = 100\,\%$ are shown in figure 6. It is clear that the fitting procedure fails to accurately describe the measured absorption around $6638.2\,\mathrm{cm^{-1}}$. This is mainly a consequence of the assumptions made

in the derivation of the absorption cross-section of HO_2 (section 3.1), namely that every transition has the same pressure-broadening parameter and, to a smaller extent, the omission of any pressure-induced shifts in our fitting procedure. It also means that the 95 % confidence intervals in figure 5 are likely to be significantly larger, since the presence of systematic errors invalidates the F-ratio technique (see discussion in section 3.2 above). More accurate spectroscopic information about HO_2 is clearly needed. We do feel, however, that the trend of $[HO_2]$ with f is reasonable (see later).

In all these measurements, the jet is oriented such that the effluent propagates horizontally (in the laboratory frame) and is orthogonal to the propagation axis of the laser beam. The laser beam intersects the plasma effluent 11 mm from the nozzle. To investigate whether HO_2 resides exclusively within the plasma effluent or not, the measurement series in figure 5 was repeated with the plasma jet being lowered relative to the laser beam and tilted downwards, passing 2 cm below the laser beam (diameter of the beam: ~ 1 mm), rather than intersecting it. To ensure the steady-state had been reached within the cavity box, each spectrum was acquired after a 15 min wait after the last curtain gas composition change while the plasma jet was switched on. The size of the HO_2 absorption was almost independent of f and corresponds to an average residual density of $[HO_2]^{bg} = 3 \times 10^{10}$ molecule cm^{-3}. This contribution requires the addition of a term $[HO_2]^{bg}\sigma_H(\nu)$ to the right-hand side of equation (1). The fit parameter, $\mathcal{N}_H$ (equation (5)), then becomes $\mathcal{N}_H = (\ell/L)[HO_2] + [HO_2]^{bg}$, from which the HO_2 number

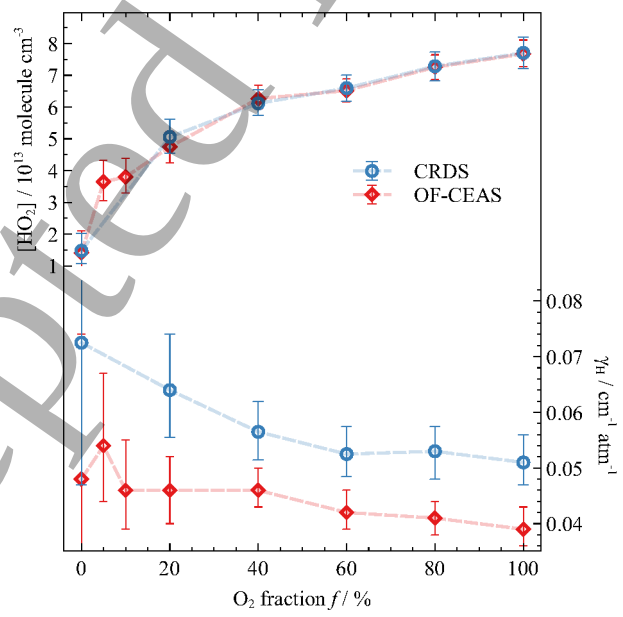

Figure 5: $[HO_2]$ and pressure-broadening parameter, γ_H, as a function of O_2 fraction in the curtain gas, f, measured with the CRDS spectrometer described in this article and with an OF-CEAS spectrometer.

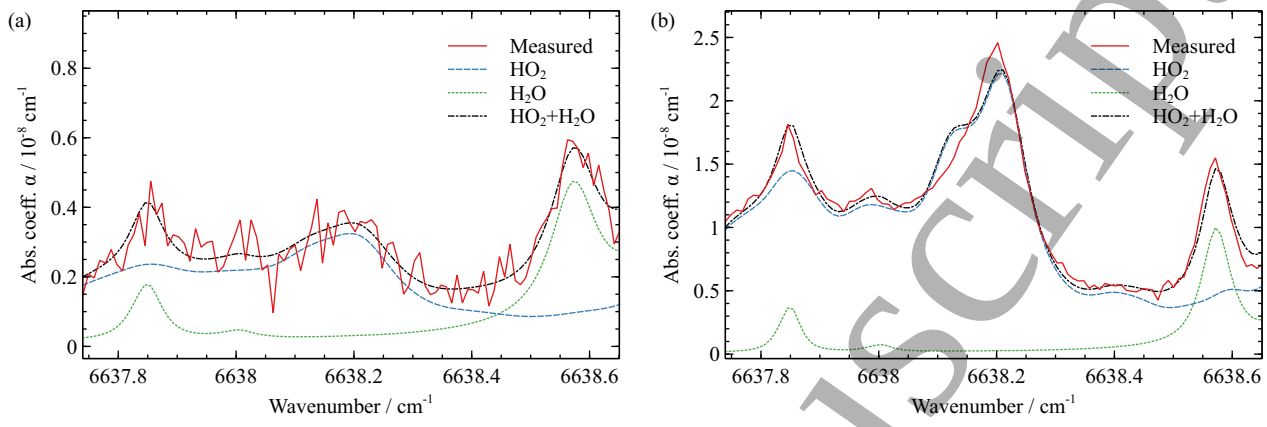

Figure 6: Absorption spectrum and fit (equation (1)) for the (a) $f = 0\,\%$ (pure N_2 curtain gas) and (b) $f = 100\,\%$ (pure O_2) measurements.

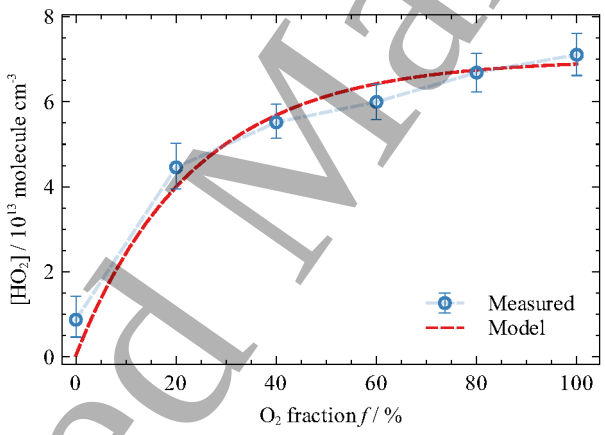

Figure 7: Measured and modeled $[HO_2]$ in the effluent as a function of oxygen fraction in the gas curtain.

density in the plasma effluent, $[HO_2]$, follows immediately ($L/\ell = 200$),

$$[HO_2] = 200(\mathcal{N}_H - [HO_2]^{bg}). \tag{13}$$

The result is shown in figure 7 together with the fit (dashed line) of the reaction kinetics model to the experimental data. The fit yields a rate coefficient $k = 8\,s^{-1}$ and a diffusion coefficient $D = 0.83\,cm^2\,s^{-1}$, which is in good agreement with the value obtained in the previous work of $D = 1\,cm^2\,s^{-1}$ [26].

Considering the uncertainty in the measured concentrations due to the large number of unknowns (accurate line centres and strengths, pressure-broadening coefficients), the assumption of a constant concentration within the diameter of the plasma effluent and zero otherwise, and the simplicity of the plug-flow model used to predict $[HO_2]$, the

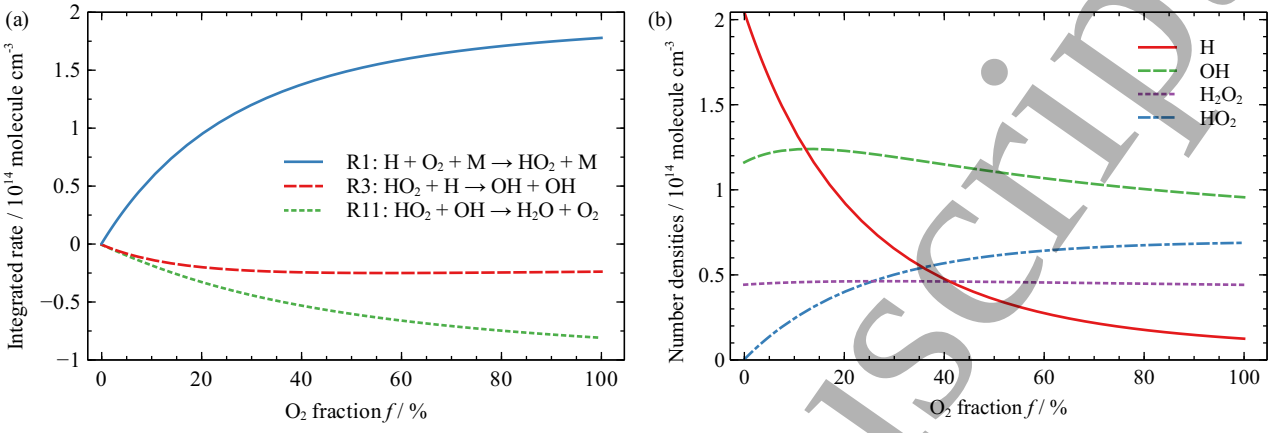

Figure 8: (a) Total [HO_2] density generated (positive values) or destroyed (negative values) by reactions (R1), (R3), and (R10) (see table 1) during the interval from 0 to 0.4 ms. (b) Number densities of relevant RONS at $t = 0.4$ ms.

agreement is reasonably good. However, it should be noted that the HO_2 density at $f = 0$ is dramatically underestimated by the model by a factor of 1/20.

Figure 8a shows the density of HO_2 generated (positive values) or destroyed (negative values) in the plasma effluent through the most important reactions listed in table 1. The data is generated by integrating the respective computed reaction rates with respect to time between $t = 0$ to 0.4 ms. Numerical simulation of the model, equation (11), shows that HO_2 is almost exclusively formed through the reaction of H and O_2 in reaction (R1). However, HO_2 is simultaneously destroyed mainly through the reaction with OH in reaction (R11), but also to a lesser extent through the reaction with H (R3); from figure 8a it is clear that roughly half of the HO_2 generated in the plasma effluent through reaction (R1) is destroyed (by (R3) and (R11)) before it can be detected. At higher HO_2 densities, the HO_2 self-reaction (R9) can be expected to contribute to a larger extent to the removal of HO_2, as the rate increases quadratically with [HO_2], possibly limiting the HO_2 density obtainable in atmospheric pressure plasma sources. As two OH molecules are generated in this reaction, this can further contribute to the HO_2 removal in reaction (R11) when more H is available. In figure 8b the calculated densities of relevant RONS at the tip of the effluent, i.e. at $t = 0.4$ ms, are given.

It is unclear, why the model underestimates HO_2 density at $f = 0$. The well-known reaction between H_2O_2 and OH (reaction (R7)) is far too slow to produce significant amounts of HO_2 in the plasma effluent. However, possible mechanisms may proceed via excited species. For example, if OH(A) is formed, the reaction with H_2O_2 could be fast enough, having a rate coefficient of 2.93×10^{-10} cm^3 s^{-1} molecule^{-1} [39].

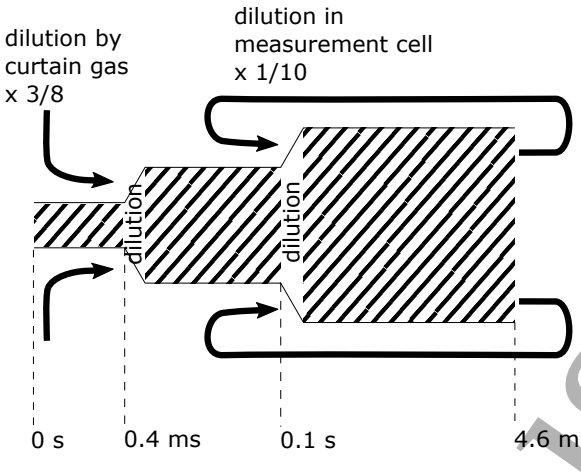

Figure 9: The plug-flow model incorporates two dilution steps, the first at 0.4 ms (corresponding to a distance of 1 cm), and the second at 0.1 s .

5.3. Downstream chemistry

The model can be employed not only for the calculation of HO_2 densities in the visible plasma effluent, but also in the measurement cell by incorporating two dilution steps as illustrated in figure 9. The first dilution is carried out after 0.4 ms. In this dilution step, all species except O_2 are diluted by a factor 3/8 to account for mixing of the feed gas with the curtain gas, i.e., a flow rate of the feed gas of 3 slm relative to the total flow rate of feed gas and gas curtain of 8 slm. O_2 is excluded from this dilution as its increase is described by equation (12). A second dilution by a factor of 1/10 is introduced after 0.1 s, in which only the highly reactive species (H, OH, and HO_2) are diluted. This second dilution step accounts for the fact that within ca. 10 cm, the total jet gas flow is further diluted by surrounding gas that entrains the jet, while the velocity of the gas rapidly drops to ca. 1 m/s. As a result the gas flow is diluted with a factor of 10 within approximately 0.1 s as previously investigated by computational fluid dynamics simulations [40]. Note that this second dilution does not decrease the total amount of RONS in the measurement cell and hence the HO_2 density needs to be multiplied by 10 again to be comparable to measurements. The main effect of this dilution is that it slows down reactions in the downstream region of the jet. It is assumed that the gas mixing with the jet flow contains orders of magnitude less H, OH, and HO_2 than the jet flow at 0.1 s, and hence their residual density is neglected. Note that this dilution step is merely introduced to investigate the longevity of HO_2 observed experimentally. The exact value of the dilution factor and the time at which the dilution takes place does not qualitatively change the results, but affects the modelled longevity of HO_2.

In figure 10 the measured residual HO_2 density is compared with the temporally averaged HO_2 density calculated from the diluted plug-flow model.

Comparing figures 7 and 10, it may be surprising that the downstream HO_2 density is hardly affected by the curtain gas composition, while a strong dependence is observed

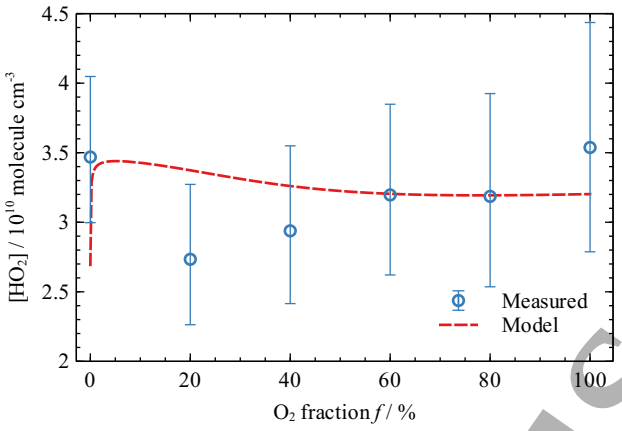

Figure 10: Measured and modeled $[HO_2]$ in the background as a function of oxygen fraction in the gas curtain

in the plasma effluent. There are two reasons for this. The first one is, that reaction (R1) is slower if less O_2 is available: as shown in figure 7b, if less O_2 is provided, more H survives as it reaches the tip of the plasma effluent. However, most of this H will form HO_2 downstream. Second, the destruction of HO_2 in the second dilution step occurs due to the self-reaction of HO_2 (reactions (R9) and (R10)). Since the rate of this process depends quadratically on the density of HO_2, the relative differences of initial HO_2 densities for different gas curtain composition are almost equalized within tens of seconds.

5.4. Low pressure measurements

Given the uncertainties associated with fitting the HO_2 spectra at atmospheric pressure, it was decided to investigate HO_2 under low pressure conditions, where spectral congestion is reduced. The plasma effluent was aimed at the pinhole mounted on the glass tube (see figure 1b). The same oxygen fraction variation series as in figure 5 was measured at 5.33 kPa and $[HO_2]$ was computed in the same way as above but neglecting the contribution to the spectra from water (figure 11). The expansion of the gas through the pinhole causes a drop in the number density, which we expect to be reduced by a factor $760/40 = 19$ compared to the initial (atmospheric pressure) value. However, the reduction is much larger; at $f = 100\,\%$ we have approximately $1.4 \times 10^{11}\,\mathrm{molecule\,cm^{-3}}$ of HO_2 at 5.33 kPa, while the atmospheric pressure measurement yields $8 \times 10^{13}\,\mathrm{molecule\,cm^{-3}}$, or a factor of 570 more. This points to very large sampling losses and possibly wall losses. Another explanation can be found in the fundamental difference between the atmospheric pressure measurements and these low pressure measurements. Although both CRDS measurements give line-of-sight numbers, the former gives the integrated number density probing the total jet diameter, while the latter is a point measurement, where only a specific location of the

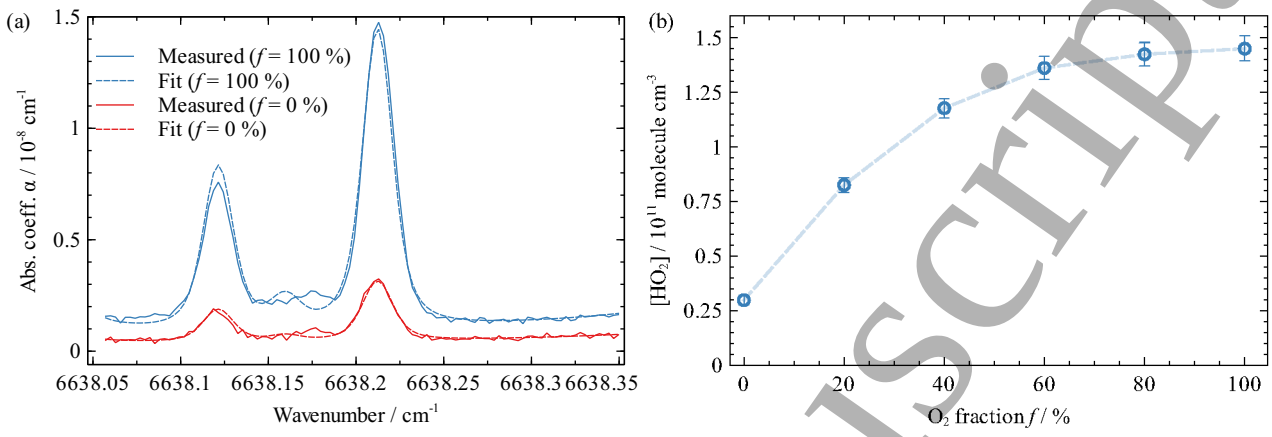

Figure 11: (a) HO_2 absorption spectra with curtain gas oxygen fraction, f, of 0 % and 100 % measured at 5.33 kPa by sampling the plasma effluent through a pinhole. (b) HO_2 number density within the cavity as a function of oxygen fraction f.

plasma effluent is sampled through the pinhole. Nevertheless, the trend of $[HO_2]$ as a function of O_2 fraction (figure 11b) is reassuringly similar to the one measured at atmospheric pressure directly in the effluent.

Sampling with a pinhole opens up the possibility of mapping the spatial distribution of HO_2 within the plasma jet. For this purpose, we translated the plasma jet device so that the effluent would sweep across the pinhole. We measured the absorption at a fixed frequency of 6638.20 cm^{-1} as a function of the displacement between measurement points of 0.13 mm. Figure 12 shows the radial profile of the HO_2 number density measured along a straight line lying in a cross-sectional plane through the plasma effluent (about 8 mm from the device's tip) for $f = 100$ % (pure O_2). Although we note that the method gives a limited spatial resolution of about 0.13 mm, this is a first indication that HO_2 is inhomogeneously distributed in the effluent of the plasma jet. This lobed structure is in contrast to previous laser-induced fluorescence measurements of the OH spatial distribution in the effluent, which shows OH to be maximally located on-axis, i.e. at 0 mm in the centre of the effluent [41]. The radial profile is expected to exhibit a strong dependence on the longitudinal position of the measurement (due to oxygen diffusion), but this was not verified here. We would like to point out that it cannot be excluded definitively that the way in which the low pressure experiment has been performed is responsible for the observed radial profile. For example, the plasma is now in contact with the surface of the pinhole and this might introduce significant deviations from undisturbed field and flow distributions. These effects have not been studied in detail in the current work. More investigations of the radial profile at low and atmospheric pressure are required, not only in longitudinal position, but also as function of the gas curtain composition, to be able to determine the spatial distribution of HO_2.

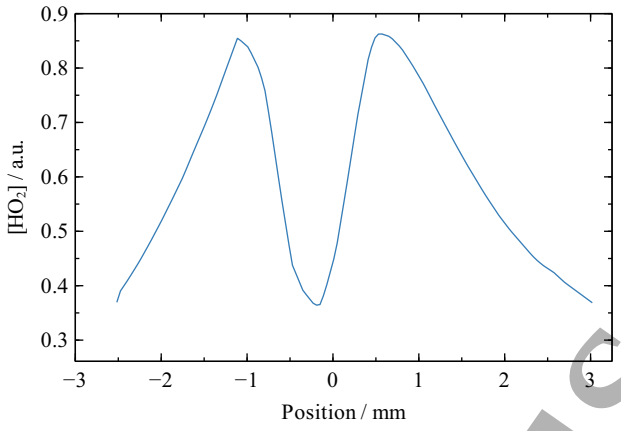

Figure 12: Radial profile of $[HO_2]$ measure at about 8 mm from the device's tip.

6. Conclusion

This work has successfully determined localized concentrations of HO_2 in the non-equilibrium atmospheric pressure plasma jet produced by a *kINPen-Sci* device equipped with a shielding gas curtain. To detect HO_2 in the plasma effluent, a cavity ring-down spectrometer with a laser source emitting at 1506.4 nm (6638.2 cm^{-1}) was employed. The detection sensitivity of the spectrometer at atmospheric pressure was 1.5×10^{11} molecule cm^{-3} of HO_2 if the absorption is assumed to be localized within 4 mm and under ideal conditions. Through a variation of the shielding gas composition in combination with a plug flow modeling approach, the trends in the experimental and theoretical HO_2 densities at 1 cm from the device's tip were compared and found to agree reasonably well, considering the uncertainties present. The model shows that most of the HO_2 is formed through the reaction of H with O_2. While a large fraction of the HO_2 is destroyed in reactions with OH and with H, it was also found that a significant fraction of HO_2 survives long enough to diffuse back into the probe beam, creating a "background" absorption signal due to HO_2 molecules residing outside of the plasma effluent. This work confirms the potential of CRDS for the study of high gradient non-equilibrium flowing systems.

Future work regarding the hydroperoxyl radical in these type of plasmas would greatly benefit from more accurate and complete spectral information on HO_2 in order to improve the uncertainties in the quantitative data. Some technical improvements – for example, to prevent the presence of the background HO_2 mentioned in the previous paragraph – are relatively easy to implement. Determination of the spatial distribution of HO_2 within (or without) the plasma effluent with the pinhole sampling technique is also of great interest.

7. Acknowledgments

This work was funded by: Natural Environment Research Council (NERC) (NE/M016439/1); Leibniz Competition 2015 (SAW-2015-INP-5); Ministry of Education, Science and Culture of the State of Mecklenburg-Vorpommern (AU15001); European Union Seventh Framework Programme FP7/2007-2013 (316216). SR would like to express his gratitude to the Alexander von Humboldt foundation.

References

[1] Penkov O V, Khadem M, Lim W S and Kim D E 2015 *J. Coat. Technol. Res.* **12** 225–235
[2] Ito M, Oh J S, Ohta T, Shiratani M and Hori M 2018 *Plasma Process Polym.* **15** e1700073
[3] Brandenburg R, Bogaerts A, Bongers W, Fridman A, Fridman G, Locke B, Miller V, Reuter S, Schiorlin M, Verreycken T and Ken K 2018 *Plasma Process Polym.* Accepted for publication, https://doi.org/10.1002/ppap.201700238
[4] Weltmann K D and von Woedtke T 2017 *Plasma Phys. Control. Fusion* **59** 014031
[5] von Woedtke T, Reuter S, Masur K and Weltmann K D 2013 *Phys. Rep.* **530** 291–320 ISSN 03701573
[6] Schmidt-Bleker A, Bansemer R, Reuter S and Weltmann K D 2016 *Plasma Process Polym.* **13** 1120–1127
[7] Reuter S, Sousa J S, Stancu G D and van Helden J P H 2015 *Plasma Sources Sci. Technol.* **24** 054001
[8] O'Keefe A and Deacon D A G 1988 *Rev. Sci. Instrum.* **59** 2544–2551
[9] Gagliardi G and Loock H P (eds) 2014 *Cavity-Enhanced Spectroscopy and Sensing* vol 179 (Berlin, Heidelberg: Springer Berlin Heidelberg) ISBN 978-3-642-40002-5
[10] Berden G and Engeln R (eds) 2009 *Cavity Ring-Down Spectroscopy: Techniques and Applications* (Oxford: Wiley-Blackwell)
[11] Lang N, Macherius U, Wiese M, Zimmermann H, Röpcke J and van Helden J H 2016 *Opt. Express* **24** A536–A543
[12] Zaplotnik R, Bišćan M, Krstulović N, Popović D and Milošević S 2015 *Plasma Sources Sci. Technol.* **24** 054004
[13] Gianella M, Reuter S, Aguila A L, Ritchie G A D and van Helden J P H 2016 *New J. Phys.* **18** 113027
[14] Djehiche M, Tan N L L, Jain C D, Dayma G, Dagaut P, Chauveau C, Pillier L and Tomas A 2014 *J. Am. Chem. Soc.* **136** 16689–16694
[15] Thiebaud J, Crunaire S and Fittschen C 2007 *J. Phys. Chem. A* **111** 6959–6966
[16] Liu Z W, Xu Y, Yang X F, Zhu A M, Zhao G L and Wang W G 2008 *J. Phys. D: Appl. Phys.* **41** 045203
[17] Tang Y, Tyndall G S and Orlando J J 2010 *J. Phys. Chem. A* **114** 369–378
[18] Bell C L, van Helden J P H, Blaikie T P J, Hancock G, van Leeuwen N J, Peverall R and Ritchie G A D 2012 *J. Phys. Chem. A* **116** 5090–5099
[19] Dünnbier M, Schmidt-Bleker A, Winter J, Wolfram M, Hippler R, Weltmann K D and Reuter S 2013 *J. Phys. D: Appl. Phys.* **46** 435203
[20] Reuter S, Winter J, Schmidt-Bleker A, Tresp H, Hammer M U and Weltmann K D 2012 *IEEE Trans. Plasma Sci.* **40** 2788–2794
[21] Winter J, Tresp H, Hammer M U, Iseni S, Kupsch S, Schmidt-Bleker A, Wende K, Dünnbier M, Masur K and Weltmann K D 2014 *J. Phys. D: Appl. Phys.* **47** 285401
[22] Rothman L S, Gordon I E, Babikov Y, Barbe A, Benner D C, Bernath P F, Birk M, Bizzocchi L, Boudon V, Brown L R, Campargue A, Chance K, Coudert L H, Devi V M, Drouin B J, Fayt A, Flaud J M, Gamache R R, Harrison J, Hartmann J M, Hill C, Hodges J T, Jacquemart D, Jolly

A, Lamouroux J, LeRoy R J, Li G, Long D, Mackie C J, Massie S T, Mikhailenko S, Müller H S P, Naumenko O V, Nikitin A V, Orphal J, Perevalov V I, Perrin A, Polovtseva E R, Richard C, Smith M A H, Starikova E, Sung K, Tashkun S A, Tennyson J, Toon G C, Tyuterev V and Wagner G 2013 *J. Quant. Spectrosc. Radiat. Transfer* **130** 4–50

[23] Ibrahim N, Thiebaud J, Orphal J and Fittschen C 2007 *J. Mol. Spectrosc.* **242** 64–69

[24] Kolobkov D, Demin O and Metelkin E 2016 *Journal of Biopharmaceutical Statistics* **26** 742–757

[25] Schmidt-Bleker A, Reuter S and Weltmann K 2015 *J. Phys. D: Appl. Phys.* **48** 175202

[26] Schmidt-Bleker A, Winter J, Bösel A, Reuter S and Weltmann K D 2016 *Plasma Sources Sci. Technol.* **25** 015005

[27] Reuter S, Winter J, Iséni S, Schmidt-Bleker A, Dünnbier M, Masur K, Wende K and Weltmann K D 2015 *IEEE Trans. Plasma Sci.* **43** 3185–3192

[28] Piper L G, Velazco J E and Setser D W 1973 *J. Chem. Phys.* **59** 3323–3340

[29] Sheldon J W and Muschlitz E E 1978 *J. Chem. Phys.* **68** 5288–5289

[30] Novicki S and Krenos J 1988 *J. Chem. Phys.* **89** 7031–7033

[31] Naidis G 2013 *Plasma Sources Sci. Technol.* **22** 035015

[32] Schmidt-Bleker A, Reuter S and Weltmann K D 2014 *Phys. Fluids* **26** 083603

[33] DeMore W B, Sander S P, Golden D M, Hampson R F, Kurylo M, Howard C J, Ravishankara A R, Kolb C E and Molina M J 1997 *JPL Publication 97-4: Chemical Kinetics and Photochemical Data for Use in Stratospheric Modeling* (Pasadena, California: Jet Propulsion Laboratory, California Institute of Technology)

[34] Baulch D L, Cobos C J, Cox R A, Esser C, Frank P, Just T, Kerr J A, Pilling M J, Troe J, Walker R W and Warnatz J 1992 *J. Phys. Chem. Ref. Data* **21** 411–734

[35] Atkinson R, Baulch D L, Cox R A, Crowley J N, Hampson R F, Hynes R G, Jenkin M E, Rossi M J and Troe J 2004 *Atmos. Chem. Phys.* **4** 1461–1738

[36] Werle P, Mücke R and Slemr F 1993 *Appl. Phys. B* **57** 131–139

[37] Buckingham A D, Disch R L and Dunmur D A 1968 *J. Am. Chem. Soc.* **90** 3104–3107

[38] Assaf E, Asvany O, Votava O, Batut S, Schoemaecker C and Fittschen C 2017 *J. Quant. Spectrosc. Radiat. Transfer* **210** 161–170

[39] McKendrick C B, Kerr E A and Wilkinson J P T 1984 *J. Phys. Chem.* **88** 3930–3932

[40] Schmidt-Bleker A, Winter J, Iseni S, Dunnbier M, , Weltmann K D and Reuter S 2014 *J. Phys. D: Appl. Phys.* **47** 145201

[41] Iseni S, Schmidt-Bleker A, Winter J, Weltmann K and Reuter S 2014 *J. Phys. D: Appl. Phys.* **47** 152001